HHS Public Access

Author manuscript

Adv Healthc Mater. Author manuscript; available in PMC 2018 February 01.

Published in final edited form as:

Adv Healthc Mater. 2017 February ; 6(4): . doi:10.1002/adhm.201601356.

Biocompatible Multifunctional Black-Silicon for Implantable Intraocular Sensor

Dr. Jeong Oen Lee[+],
Department of Medical Engineering, California Institute of Technology, Pasadena, CA, 91106, (USA). Department of Electrical Engineering, California Institute of Technology, Pasadena, CA, 91106, (USA)

Vinayak Narasimhan[+],
Department of Medical Engineering, California Institute of Technology, Pasadena, CA, 91106, (USA)

Dr. Juan Du,
Department of Ophthalmology, University of California, San Francisco, San Francisco, CA, 94143, (USA)

Dr. Blaise Ndjamen,
Department of Medical Engineering, California Institute of Technology, Pasadena, CA, 91106, (USA)

Prof. David Sretavan, and
Department of Ophthalmology, University of California, San Francisco, San Francisco, CA, 94143, (USA)

Prof. Hyuck Choo[*]
Department of Medical Engineering, California Institute of Technology, Pasadena, CA, 91106, (USA). Department of Electrical Engineering, California Institute of Technology, Pasadena, CA, 91106, (USA)

Graphical Abstract

Multifunctional black silicon (b-Si) integrated on the surface of an implantable intraocular pressure (IOP) sensor significantly improves sensor performance and reliability in 6-month *in-vivo* studies. The anti-reflective properties of b-Si triples the signal-to-noise ratio and increases the optical readout distance to a clinically viable 12 cm. Tissue growth and inflammation response on the sensor is suppressed demonstrating desirable anti-biofouling properties.

[*]Corresponding-Author: Prof. H. Choo, hchoo@caltech.edu.
[+]These authors contributed equally to this work

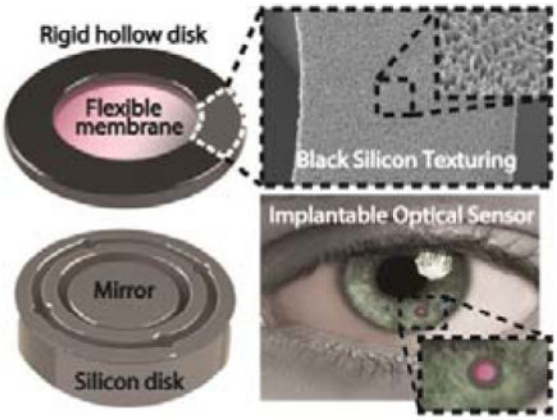

Keywords

optical readout; intraocular pressure (IOP); black-silicon; in-vivo monitoring; glaucoma

Burgeoning research on implantable medical microdevices has been actively driving the development of multifunctional biomaterials to improve device performance and reliability [1–5]. Black silicon (b-Si) or nano-grass, a textured silicon (Si) surface with micro- and nanoscale high aspect-ratio topologies, is known to possess highly useful surface properties [6–8] and has been used in a myriad of applications such as in light-absorbing anti-reflection layers in photovoltaics and surface-enhanced Raman scattering [9–12], bonding layers in microelectromechanical systems (MEMS) [13], liquid-guiding layers in microfluidics [14, 15], and bio-inspired/mimetic functional surfaces [16]. In the current work, we demonstrated the use of b-Si as an anti-reflection and anti-biofouling layer on an optically probed implantable intraocular pressure (IOP) sensor and significantly improved its optical performance and long-term *in-vivo* biocompatibility and reliability. The b-Si enabled IOP monitoring at 12 cm on fully awake rabbits, the largest readout distance reported to our knowledge [17–20] (Fig. 1), and demonstrated remarkable antifouling properties analogous to biological nanostructures found in nature [11, 21, 22], preventing encapsulating tissue growth on the implant. To our knowledge, this is the first *in-vivo* demonstrated use of b-Si as a multifunctional biomaterial on an implantable medical sensor.

The implantable IOP sensor recently reported is a microscale optical cavity made of two separate parts: a deformable transparent silicon-nitride (Si_3N_4) membrane on top of a reflective Si surface, separated by a 4-μm air gap (Fig. S1a) [23]. The top and bottom parts are fabricated individually and assembled under a microscope using medical grade epoxy to form a hermetically sealed optical cavity at 1 atm. The pressure difference between the interior and exterior of the cavity deflects the flexible membrane and changes the size of the gap, consequently shifting the cavity's optical resonance. To measure IOP, broadband near-infrared (NIR) light generated by a tungsten bulb is exposed onto the core cavity of the sensor implanted inside the anterior chamber of the eye through a tabletop microscope at 2–3 cm, and a commercially available mini-spectrometer connected to the microscope is used to detect the reflected optical resonance spectrum and convert it to the corresponding IOP

level (Fig. S1b) [24]. *In-vivo* measurements using this system require test animals to be under anesthesia.

A more practical IOP-sensing approach demands for the adaptation of easy-to-use readout systems such as a common ophthalmic microscope. This requires a longer optical readout distance and an expanded field-of-view, which inevitably increase background noise detection. The noise reflected from the cornea, lens, iris, or aqueous humor are not significant because of their low reflectivities, about 3% or smaller [25]. However, the inactive region of the sensor is a highly reflective Si surface and is coaxially aligned with the detector (Fig. 1b), generating strong background noise and degrades the SNR of the sensor.

In order to suppress the background noise from the inactive regions of the sensor, anti-reflective b-Si was integrated on the inactive region of the sensor (Fig. 1b, 1c). The b-Si effectively scatters incoming light and significantly increases its absorption [26, 27]. A room-temperature b-Si process was developed using a mixed-mode plasma etch, which did not require an expensive cryogenic setup or a time-consuming cooling process (Fig. 2) [26–32]. The b-Si growth was seamlessly integrated with the existing IOP sensor fabrication process (Fig. S3) [23, 24]. Varying the process conditions, b-Si nanostructures were successfully optimized to obtain the anti-reflection properties in the wavelength range of interest (Fig. 2a, b, c; Fig. S2). Integrating the b-Si on the inactive region lowered reflectivity down to 10% of a polished Si surface and produced 3.5% absolute reflectivity (Fig. 2d, e, f; Fig. S3). This improvement in the signal-to-noise ratio (SNR) allowed a slit-lamp, the most commonly utilized clinical ophthalmic microscope, to be used as a readout system and accomplish *in-vivo* IOP monitoring on rabbits that were fully awake.

IOP sensing performance of b-Si-integrated and Si-only IOP sensors with identical dimensions were examined using a tabletop microscope and a slit-lamp (Fig. 3a). The first captured signals were from the 600 μm wide active core cavities of the sensors, excluding the inactive regions, using a microscope (20x objective) at a readout distance of 3 cm. The resonance spectra from the two sensors were almost identical and of good quality (Fig. 3b). The outer envelope of the captured spectrum is determined by the blackbody radiation of the tungsten light source, NIR filters in the detector, and the thickness of Si_3N_4 membrane, while higher frequency peaks and valleys inside the envelop are determined by the optical cavity with an air gap between the Si_3N_4 membrane and the Si substrate. A mini-spectrometer and a CCD camera were connected onto the slit-lamp's two expansion ports (Fig. S5) allowing spectra to be captured at 12 cm, the largest readout distance reported to our knowledge [17–20]. The increased field-of-view (2×2 mm^2) included the sensor's active core cavity and the surrounding inactive region. While the quality of resonance spectra captured from the b-Si sensor were hardly influenced by the inclusion of the surrounding regions, the SNR of the resonance spectra captured from the Si-only sensor decreased by 71%, below 10 dB, due to the highly reflective inactive region of the sensor (Fig. 3c).

Next, using a pressure-controlled test chamber (range: 0–40 mmHg, step size: 0.5 mmHg) interfaced with a digital pressure gauge and applying the slit-lamp measurement conditions, the IOP measurement accuracy was determined. When compared to the digital pressure

gauge, measurements using the Si-only sensor showed considerable fluctuations (Fig. 3d): the root-mean-square error (RMSE) and the peak-to-peak fluctuation were 1.96 and ±8 mmHg, respectively (Fig. 3e). In contrast, measurements using the b-Si sensor exhibited an RMSE of 0.58 mmHg and peak-to-peak variation less than ±2 mmHg over the entire pressure range (Fig. 3g), which would satisfy the clinically accepted error range of ±2 mmHg [33].

For *in-vivo* tests using the modified slit-lamp as the readout system (Fig. 4b and Fig. S5), each sensor was individually mounted on a thin, flexible silicone strip and implanted into the anterior chambers of two New Zealand white rabbits (Fig. 4a). For each IOP measurement, the top 30 highest SNR spectra from a set of continuously captured 600–1800 spectra (measurement time: 1–3 minutes, resolution bandwidth: 10Hz) were averaged to improve accuracy. All IOP measurements were performed on fully awake rabbits.

The resonance spectra of the b-Si sensor shown in Fig. 4d fluctuated less than ±1 nm (Supplementary Information), and the corresponding IOP was 7.3 mmHg. In contrast, it was impossible to identify peak-and-valley locations from the resonance spectra of the Si-only sensor and calculate the IOP (Fig. 4e). For reference, b-Si sensor measurements were compared with those made using tonometry (TonoVet, ±2-mmHg accuracy) for three months (Fig. 4f). The IOP measurements using the b-Si sensor generally paralleled the tonometer readouts, however the average standard deviation of the b-Si-sensor measurements was much smaller, 0.48 mmHg vs. 1.45 mmHg for the tonometer measurements. In addition, the b-Si sensor showed no sign of performance degradation, constantly maintaining a SNR over 10 dB for 3 months (Fig. 4g).

To investigate the extent of surface fouling and its influence on the sensor reliability, Si-only and b-Si IOP sensors that had been implanted for more than 6 months were harvested. Confocal immunofluorescence microscopy was performed on the sensors to determine cell and tissue viability at the time of extraction (Supplementary Information). The amount of F-actin present in the cytoskeleton of eukaryotes was used as an indicator of cellular processes and health, and provided evidence to predict cell-and-tissue encapsulation of the implant [34]. DAPI 405 (cell nucleus marker), Phalloidin 555 (cell F-actin marker), and CD62L 488 (L-selectin inflammation marker) in the extracted sensors were counter-stained and scanned from the surface of the inactive region down to the top of the Si_3N_4 membrane along the *z*-axis (step: 2.5 μm, scan range: 300 μm, Zeiss LSM 880, 10x EPI objective) (Fig. S7a).

Fig. 4h and *i* present the results of the z-stack imaging performed on the Si-only and b-Si sensors, respectively, and illustrate the extent of tissue growth. On the Si-only sensor, the cells extended from the inactive region onto the active (Si_3N_4 membrane surface) region, covering about 62% of the active area, and contained large F-actin filaments, which implied the adherent cells were growing healthily at the time of extraction (Fig. 4h, Fig. S6b). This is highly undesirable because dense tissue growth would ultimately block the optical pathway of the sensor and alter its mechanical properties. In addition, imaging with CD62L 488 indicated several instances of inflammation within a tight cluster of cells covering the Si_3N_4 membrane (Fig. S8).

In contrast, the b-Si sensor showed almost no sign of tissue growth or discernable onset of encapsulation (Fig. 4i and k). Only 5% of the active region was covered by tissue (Fig. S7b) and non-specific bindings of fluorophores were seen on the b-Si surface in the form of a partial ring (Fig. 4i). The surface-area ratio of Phalloidin 555 to DAPI 405 was 3.3 for the b-Si sensor, approximately four times smaller than the Si-only sensor (13.3). This indicates that most of the cells on the b-Si sensor were unhealthy and F-actin-deficient, experiencing de-polymerization whereby filamentous F-actin disassociates into its globular G-actin [35, 36]. This leads to degeneration and thus deters any further growth or encapsulation.

The highly non-uniform surface of b-Si is postulated to prevent cell adhesion and therefore inhibit tissue-encapsulation of the implant. Furthermore, no instances of inflammation were observed on the b-Si sensor (Fig S8), which correlates with the recent findings indicating the biocompatibility of b-Si surfaces in the presence of eukaryotes [37]. Further studies are currently underway to better understand the biophysical interaction of b-Si within the ocular environment and its antifouling properties for implant applications in general.

In summary, using b-Si as a multifunctional material on the IOP-sensing medical implant significantly improved the sensor performance and reliability. The b-Si was fabricated using a newly developed room-temperature process, which seamlessly integrated with the fabrication steps of the implantable IOP sensors. The anti-reflective properties of b-Si reduced the background noise of the sensor and allowed adaption of a slit-lamp, the most commonly used clinical ophthalmic microscope, as a readout system during *in-vivo* IOP monitoring. B-Si effectively suppressed tissue growth on the surface of the implant over a six-month period, promising significantly improved long-term reliability of the implant. The demonstrated improvement in both performance and reliability enabled *in-vivo* studies on fully awake rabbits for six months, positive indications of the possibility of realizing our IOP-sensing approach for everyday use. Further miniaturization of the sensor and improvement of the sensor-securing mechanism inside the eye will greatly simplify the insertion procedure and enhance patient comfort. Furthermore, additional studies will be conducted in the future to elucidate the underlying mechanisms of the presented work and the long-term effect of b-Si inside the eye, which will ultimately allow us to demonstrate the full potential of b-Si as a multifunctional biomaterial for medical implants.

Experimental Section

B-Si Fabrication at Room Temperature

A reactive-ion-etching (RIE) process (Oxford Instruments System 100 ICP 380) was used to fabricate the wafer-scale b-Si surface. The process chamber was maintained at 20°C, while the flow rates of SF_6 and O_2 gas were set at 47 and 44 sccm, respectively. The etching process was conducted in multiple steps to tune the reflectivity (Fig. 2a). Integration of the b-Si process into the IOP-sensor fabrication is described in Fig. S4.

Characterization of the B-Si IOP Sensor

Two measurement setups were used: (1) a tabletop optical microscope equipped with a CCD camera (ThorLabs), a broadband light source (Ocean Optics HL-2000), and a spectrometer

(Ocean Optics Maya2000 Pro-NIR); and (2) a slit-lamp integrated with a CCD (Thorlabs) and a spectrometer (Ocean Optics Maya2000 Pro-NIR) using two of the slit-lamp's expansion ports [24]. For slit-lamp measurements, the spectra were collected using the built-in tungsten bulb and optics (L1, L2, and a beam splitter, wherein L2 is configurable to four different magnifications (5x, 8x, 10x and 30x), Fig. 4c).

To calculate IOPs, an in-house-developed program was used to identify and convert the locations of the peaks and valleys in a captured spectrum into the corresponding size of the cavity gap and external pressure [38]. The reference pressures inside the test chamber were obtained using a commercial digital pressure gauge (1210 Pressure Sensor, TE Connectivity Ltd.) with ±0.1 mmHg accuracy.

Continuous In-Vivo IOP Monitoring in Unanesthetized Rabbits

Each IOP sensor was mounted on a 200 μm wide and 2.5 mm long flexible "I"-shaped silicone strip and inserted into the anterior chamber of the rabbit eye through a 2-mm corneal incision [24]. The sensor-mounted strip was positioned over the iris and the crystal lens and secured against the inner walls of the cornea (Fig. 4a).

In-vivo measurements were performed using a modified slit-lamp (Fig. 4b). Using the built-in eye piece or the CCD camera (Fig. S5), the sensor was located by setting L2 at its lowest magnification. The optical alignment between the sensor and the detection system was easily accomplished using the slit-lamp's built-in translational stage (4 degrees of freedom, 3 translational and 1 rotational). The L2 magnification was then increased to 30x and the active region of the sensor occupied ~9.6% of the field of view (Fig. 4a). A single spectrum required 100 ms to capture.

Confocal Immunofluorescence Microscopy and Analyses

A detailed description of the sample preparation protocol for the confocal immunofluorescence imaging is provided in the Supplementary Information. Surface area measurements (DAPI 405 and Phalloidin 555, Fig. S7b) and inflammatory response (CD62L 488, Fig. S8) were determined over the sensors' core cavity regions using ImageJ, an open-source image-processing program. Inflammatory response assessment was conducted by studying the overlap between DAPI 405 and CD62L 488.

Supplementary Material

Refer to Web version on PubMed Central for supplementary material.

Acknowledgments

The work was funded by the National Institute of Health (NIH) EY024582, HMRI Investigator Award, Caltech CI2 program, and Powell Foundation Award. (Supporting Information is available online from Wiley InterScience or from the authors).

References

1. Canales A, Jia X, Froriep UP, Koppes RA, Tringides CM, Selvidge J, Lu C, Hou C, Wei L, Fink Y, Anikeeva P. Nat Biotech. 2015; 33:277.

2. Acarregui A, Herrán E, Igartua M, Blanco FJ, Pedraz JL, Orive G, Hernandez RM. Acta Biomater. 2014; 10:4206. [PubMed: 25010523]
3. Thoniyot P, Tan MJ, Karim AA, Young DJ, Loh XJ. Adv Sci. 2015; 2:1400010.
4. DeMuth PC, Min Y, Irvine DJ, Hammond PT. Adv Healthc Mater. 2014; 3:47. [PubMed: 23847143]
5. Mendes RG, Bachmatiuk A, Büchner B, Cuniberti G, Rummeli MH. J Mater Chem B. 2013; 1:401.
6. Stubenrauch M, Fischer M, Kremin C, Stoebenau S, Albrecht A, Nagel O. J Micromech Microeng. 2006; 16:S82.
7. Jansen HV, de Boer MJ, Unnikrishnan S, Louwerse MC, Elwenspoek MC. Micromech Microeng. 2009; 19:1.
8. Jansen H, de Boer M, Legtenberg R, Elwenspoek M. Micromech Microeng. 1995; 5:115.
9. Otto M, Kroll M, Käsebier T, Lee SM, Putkonen M, Salzer R, Miclea PT, Wehrspohn RB. Adv Mater. 2010; 22:5035. [PubMed: 20859945]
10. Yoo J, Yu G, Yi J. Sol Energy Mater Sol Cells. 2011; 95:2.
11. Ziegler J, Haschke J, Käsebier T, Korte L, Sparfke AN, Wehrspohn RB. Opt Express. 2014; 22:A1469. [PubMed: 25607304]
12. Gervinskas G, Seniutinas G, Hartley JS, Kandasamy S, Stoddart PR, Fahim NF, Juodkazis S. Ann Phys. 2013; 525:907.
13. Stubenrauch M, Fischer M, Kremin C, Hoffmann M, Müller J. Micro Nano Lett. 2007; 2:6.
14. Dorrer C, Rühe J. Adv Mater. 2008; 20:159.
15. Barberoglou M, Zorba V, Pagozidis A, Fotakis C, Stratakis E. Langmuir. 2010; 26:13007. [PubMed: 20593795]
16. Ivanova EP, Hasan J, Webb HK, Gervinskas G, Juodkazis S, Truong VK, Wu AHF, Lamb RN, Baulin VA, Watson GS, Watson JA, Mainwaring DE, Crawford RJ. Nat Comm. 2013; 4(2838):1.
17. Chen PJ, Rodger DC, Saati S, Humayun MS, Tai YC. J Microelectromech. 2008; 17:1342.
18. Araci AE, Su B, Quake SR, Mandel Y. Nat Med. 2014; 20:1074. [PubMed: 25150497]
19. Xue N, Chang SP, Lee JB. J Microelectromech. 2012; 21:1338.
20. Todani A, Behlau I, Fava MA, Cade F, Cherfan DG, Zakka FR, Melki SA. Invest Ophthalmol Vis Sci. 2011; 52:9573. [PubMed: 22039243]
21. Ivanova EP, Hasan J, Webb HK, Truong VK, Watson GS, Watson JA, Baulin VA, Pogodin S, Wang JY, Tobin MJ, Lobbe C, Crawford RJ. Small. 2012; 8:2489. [PubMed: 22674670]
22. Pogodin S, Hasan J, Baulin VA, Webb HK, Truong VK, Nguyen THP, Boshkovikj V, Fluke CJ, Watson GS, Watson JA, Crawford RJ, Ivanova EP. Biophys J. 2013; 104:835. [PubMed: 23442962]
23. Lee JO, Nguyen TT, Stretavan D, Choo H. PIERS Proc. 2014:826.
24. Lee JO, Park H, Chen O, Balakrishna A, Du J, Sretavan DW, Choo H. Proc IEEE Int Conf MEMS. 2016:210.
25. Hecht, E. Optics. 5. Pearson; New York, USA: 2016.
26. Gaudig M, Hirsch J, Schneider T, Sprafke AN, Ziegler J, Bernhard N, Wehrspohn RB. J Vac Sci Technol A. 2015; 33:05E132–1.
27. Koynov S, Brandt MS, Stutzmann M. Appl Phys Lett. 2006; 88:203107–1.
28. Schnell, M., Lüdemann, R., Schaefer, S. 28th IEEE Photovoltaic Specialists Conference; Anchorage, Alaska. 2000; p. 367
29. Zaidi SH, Ruby DS, Gee JM. IEEE Trans Electron Devices. 2001; 48:1200.
30. Otto M, Kroll M, Käsebier T, Salzer R, Tünnermann A, Wehrspohn RB. Appl Phys Lett. 2012; 100:191603.
31. Repo P, Benick J, Vähänissi V, Schön J, von Gastrow G, Steinhauser B, Schubert MC, Hermle M, Savin H. Energy Procedia. 2013; 38:866.
32. von Gastrow G, Alcubilla R, Ortega P, Yli-Koski M, Conesa-Boj S, Morral AFi, Savin H. Sol Energy Mater Sol Cells. 2015; 142:29.
33. Kontiola A, Puska P. Graefes Arch Clin Exp Ophthalmol. 2004; 242:3. [PubMed: 14634828]
34. Dominguez R, Holmes KC. Annu Rev Biophys. 2011; 40:169. [PubMed: 21314430]

35. Pollard TD, Cooper JA. Science. 2009; 326:1208. [PubMed: 19965462]
36. Holmes KC. Nature. 2009; 457:389. [PubMed: 19158779]
37. Pham VTH, Truong VK, Orlowska A, Ghanaati S, Barbeck M, Booms P, Fulcher AJ, Bhadra CM, Buividas R, Baulin V, Kirkpatrick CJ, Doran P, Mainwaring DE, Juodkazis S, Crawford RJ, Ivanova EP. ACS Appl Mater Interfaces. 2016; 8:22025. [PubMed: 27494044]
38. Hill GC, Melamud R, Declercq FE, Davenport AA, Chan IH, Hartwell PG, Pruitt BL. Sensors and Actuators A. 2007; 138:52.

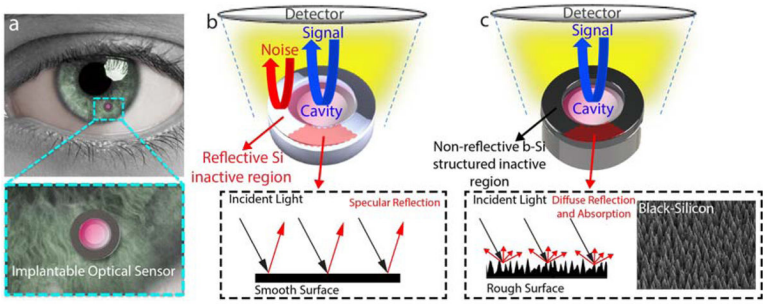

Figure 1. b-Si structured IOP sensor

(a) Conceptual illustration of the implantable IOP sensor with a microscale optical cavity and a zoomed-in image. **(b)** A Si-only sensor consisting of an active core cavity and a reflective peripheral inactive region. Reflection arises from both the cavity (shown in blue) and the Si (shown in red). **(c)** A b-Si sensor with integrated b-Si on the inactive hollow disk. Only the reflection from the core cavity is captured. The inset is a SEM image of the b-Si grown on the inactive region.

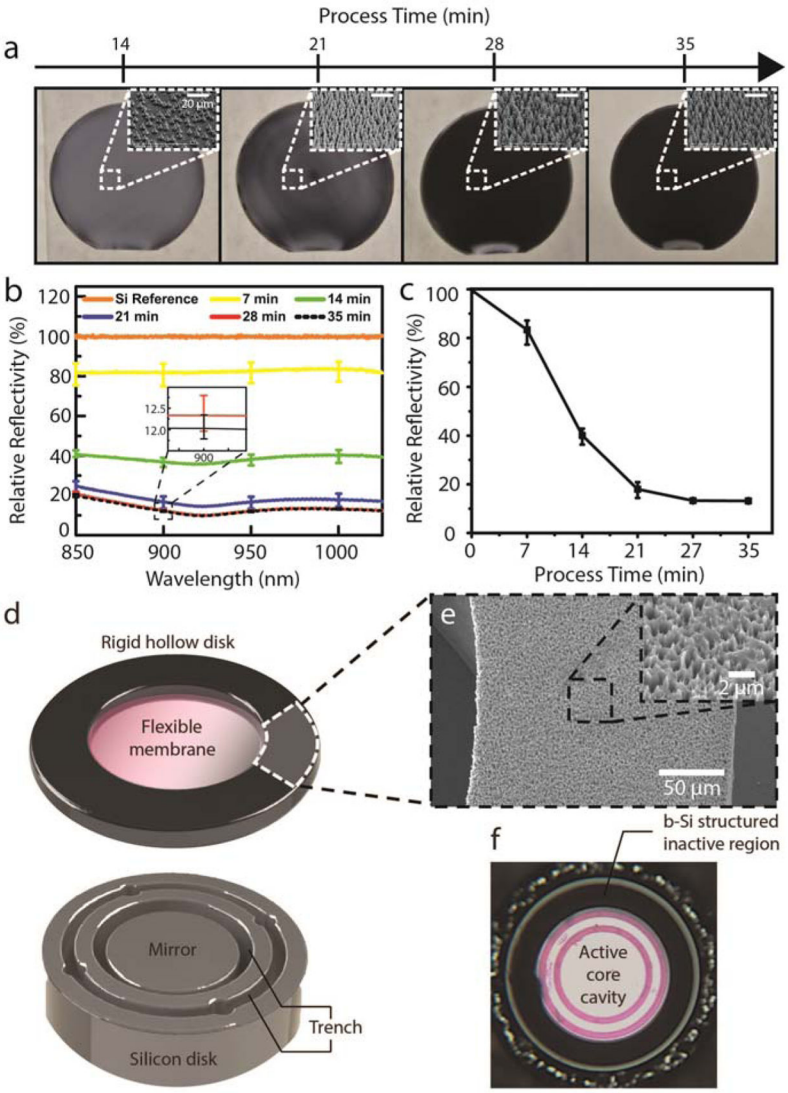

Figure 2. b-Si process development and IOP sensor integration

(a) Wafer-scale b-Si process performed on 6-inch wafers (insets: SEM images taken at 45°; scale: 20 μm). **(b)** Relative reflectivity of b-Si surface vs. the wavelength range of interest for 5 different process durations (5-point measurements). The inset shows a zoomed-in image of the error bars for 28- and 35-minute process times. **(c)** Wavelength-averaged relative reflectivity vs. process time. **(d)** b-Si textured inactive region on the top and a Si mirror on the bottom. **(e)** SEM image of the b-Si-textured inactive region. Scale bar: 50 μm. Inset: magnified SEM image of the b-Si surface. Scale: 2 μm. **(f)** A photograph of an assembled IOP sensor with the b-Si-textured inactive region.

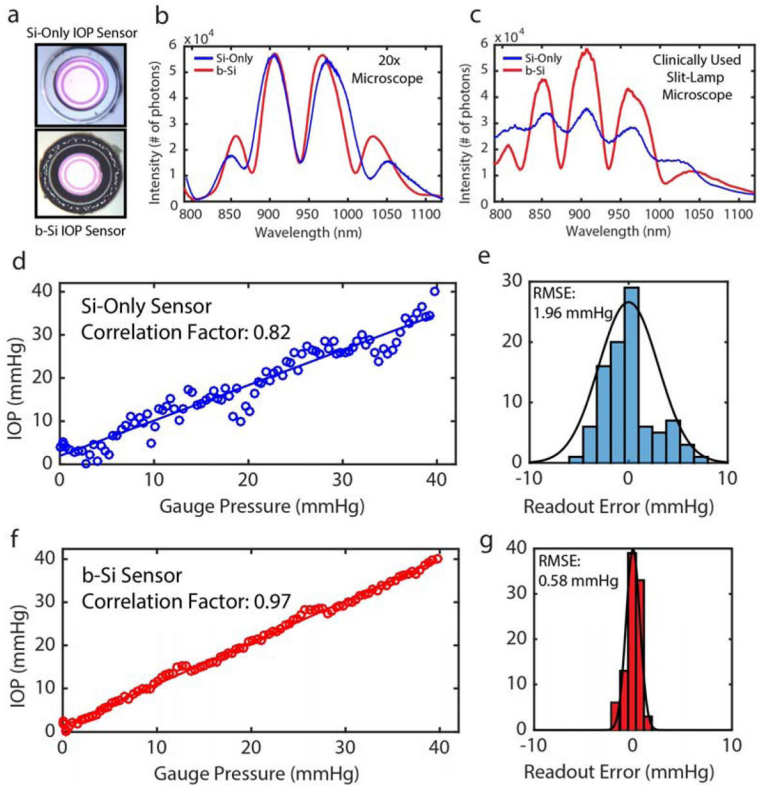

Figure 3. b-Si and Si-only IOP Sensor Characterization

(a) Fabricated Si-only (top) and b-Si (bottom) sensors. **(b)** Spectral measurements using a tabletop microscope with a 20x objective lens (field-of-view: 800×800 μm^2, working distance: 3 cm). **(c)** Spectral measurements using a slit-lamp (size of the field of the view: 2 x 2 mm^2; working distance: 12 cm). **(d)** IOP measurements using the Si-only sensor. **(e)** Readout-error distribution of the Si sensor. **(f)** IOP measurements using the b-Si sensor. **(g)** Readout-error distribution of the b-Si sensor.

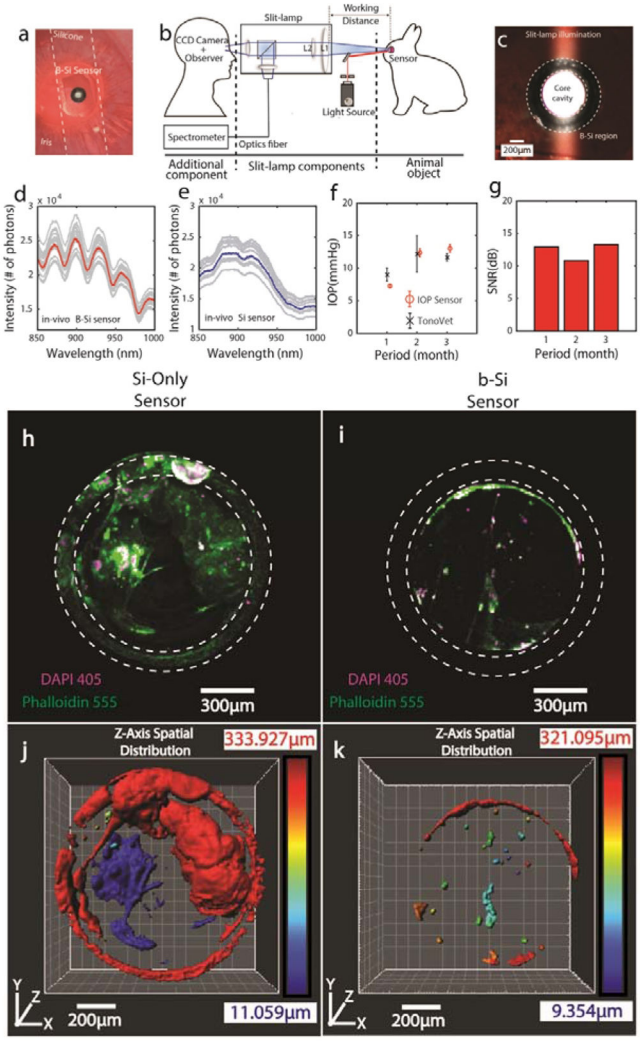

Figure 4. ***In-Vivo*** **IOP Monitoring of Unanesthetized Rabbits**

(a) A photo of the b-Si sensor implanted inside a rabbit eye using a flexible silicone strip. **(b)** A modified slit-lamp readout system. **(c)** A photo of the illuminated sensor in the rabbit eye taken using a slit-lamp at 30x magnification. Top 30 highest-SNR *in-vivo* spectra (gray curves) selected out of 600–1800 measurements from the b-Si sensor **(d)** and Si-only sensor **(e)**, captured at 1 month following the implantation. Corresponding means: red (b-Si sensor) and blue (Si-only sensor) curves. **(f)** IOP measurements using the b-Si sensor and a TonoVet. **(g)** SNRs of the b-Si sensor over 3 months. 3D-confocal z-stack images (Zeiss LSM-880 confocal microscope) of the Si-only sensor **(h)** and the b-Si sensor **(i)** harvested more than 6 months after implantation (DAPI: purple channel, nucleus; Phalloidin: green channel, F-actin; step size: 2.5 μm; scan range: 300 μm) (Fig. S7). 3D reconstruction (Imaris, Bitplane Inc.) showing the spatial distributions of tissues adherent on the Si-only sensor **(j)** and the b-Si sensor **(k)**. The color bar indicates the vertical location of the tissue along the *z*-axis, with blue indicating the top of the Si_3N_4 membrane.